IEEE Photonics Journal
An IEEE Photonics Society Publication

Open Access

Machine-Learning Classification of Port Wine Stain With Quantitative Features of Optical Coherence Tomography Image

Volume 11, Number 6, December 2019

Shengnan Ai
Chengming Wang
Wenxin Zhang
Wenchao Liao
Juicheng Hsieh
Zhenyu Chen
Bin He
Xiao Zhang
Ning Zhang
Ying Gu
Ping Xue

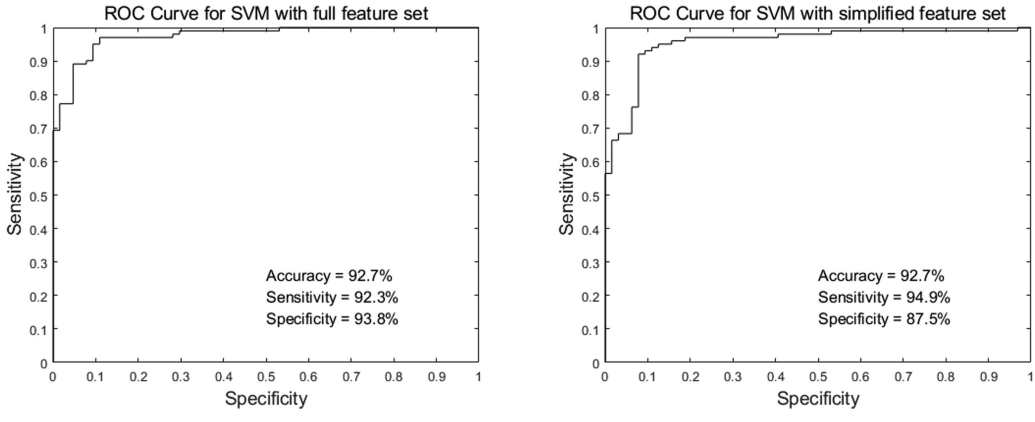

DOI: 10.1109/JPHOT.2019.2952903

Machine-Learning Classification of Port Wine Stain With Quantitative Features of Optical Coherence Tomography Image

Shengnan Ai,[1,6] **Chengming Wang**,[1,2,6] **Wenxin Zhang**,[1,6] **Wenchao Liao**,[1,6] **Juicheng Hsieh**,[1,6] **Zhenyu Chen**,[1,6] **Bin He**,[1,6] **Xiao Zhang**,[3] **Ning Zhang**,[4] **Ying Gu**,[5] **and Ping Xue**[1,6]

[1]State Key Laboratory of Low-Dimensional Quantum Physics, Department of Physics, Tsinghua University, Beijing 100084, China
[2]Nuctech Company, Ltd., Beijing 100084, China
[3]School of Life Science, Beijing Institute of Technology, Beijing 100081, China
[4]Institute of Forensic Science, Ministry of Public Security, Beijing 100038, China
[5]Department of Laser Medicine, Chinese PLA General Hospital, Beijing 100853, China
[6]Collaborative Innovation Center of Quantum Matter, Beijing 100084, China

DOI:10.1109/JPHOT.2019.2952903

Manuscript received October 31, 2019; accepted November 6, 2019. Date of publication November 11, 2019; date of current version December 16, 2019. This work was supported in part by the National Natural Science Foundation of China under Grants 61227807, 61575108, and 61505034, and in part by Tsinghua Initiative Scientific Research Program under Grant 2013THZ02-3. *(Shengnan Ai and Chengming Wang contributed equally to this work.)* Corresponding author: Ping Xue (e-mail: xuep@tsinghua.edu.cn).

Abstract: Port wine stain (PWS) is the benign congenital capillary malformation of skin, occurring in 0.3% to 0.5% of the population. In this paper, we build two automated support vector machine (SVM) based classifiers by extracting quantitative features from normal and PWS tissue images recorded by optical coherence tomography (OCT). We use both full feature set and simplified feature set for training. Accuracy of 92.7%, sensitivity of 92.3% and specificity of 93.8% were obtained for classifier with full feature set. Accuracy of 92.7%, sensitivity of 94.9% and specificity of 87.5% were obtained for classifier with simplified feature set. Our results suggest that extracting quantitative features from optical coherence tomographic images could be a potentially powerful method for accurately and automatically identifying PWS margins during laser therapy.

Index Terms: Port wine stain, optical coherence tomography, machine learning.

1. Introduction

Port wine stain (PWS) is the congenital capillary malformation of skin, occurring in 0.3% to 0.5% of the population [1]. Most lesions initially appear as flat, pink to purple patches. They may progress into hypertrophic, nodular, dark red to dark purple patches with age [2]. About 70% to 80% of PWS occurs in the head and neck regions, which may significantly impact a person's mental health [3]–[5]. Thus, many patients may seek for treatment. Radiation therapy, freezing, surgical excision, and tattooing used to be performed for PWS treatment [6]. Nowadays, laser therapy systems become popular because of their abilities to destroy cutaneous vessels while preserving the normal vessels. Among all laser systems, Pulsed dye laser (PDL) remains the clinical gold standard. PDL works by selective photo-thermolysis and about 50% to 70% color reducing of

the PWS is achieved [7]. During PDL therapy, the laser spot size, laser power and pulse duration should be chosen properly and the treatment area should be limited to target lesions [6]. Undersized treatment spot may not be able to get completely clearance. Patients need more sessions, which is time-consuming and costly. However, oversized treatment spot may cause skin inflammation, pigmentation defects and scar. Doctors usually discriminate between normal and PWS skin by color in clinical practice. During the treatment, we found that some of the patients' lesion colors were reduced to normal, while the corresponding OCT images still showed enlarged distorted blood vessels. If the treatment is stopped at this stage, the distorted blood vessels will expand with age and the color will turn red again [8], [9]. In order to prevent such regeneration and revascularization, the treatment should continue on the skin lesions that were reduced to normal color. Therefore, an objective assessment of PWS tissue margin is needed, especially without the help of an expert clinician. Several imaging modalities have been developed for PWS assessment such as laser speckle imaging [10], reflectance spectrophotometers [11], reflectance confocal microscopy (RCM) [12], tristimulus colorimeters [13], cross-polarized diffuse reflectance (CDR) color imaging [14], laser Doppler flowmetry (LDF) [15], spatial frequency domain imaging (SFDI) [16] and optical coherence tomography (OCT) [17].

Optical coherence tomography (OCT) is a high-resolution, non-invasive, cross-sectional imaging modality first developed in 1991 [18]. With development, OCT has shown the potential to provide clinical benefits in dermatology, which can be used in diagnosis of skin diseases and monitoring of treatment effects [19]. Several machine learning algorithms were applied in OCT images for automatically diagnosis of skin diseases, such as linear regression [25], support vector machine (SVM) [28], [31], k-nearest neighbor (KNN) [29], random forest [30]. In our previous work, we try to use OCT as a tool for the treatment monitor in PWS [17], [20], [21]. A pilot machine learning study for PWS diagnosis was undertook by Bazant-Hegemark F., *et al.* [32]. 96 synthesized images and 7 clinical images were used. Classification accuracy of 99.8% in synthesized images and 71.4% in clinical images were achieved. In this paper, we trained two SVM classifiers with quantitative features extracted from OCT images. The same OCT system is used for clinical image collection as our previous work [17]. In our study, 140 normal samples and 80 PWS samples were used. Thirteen quantitative features were extracted as full feature set. Simplified feature set was built by excluding the features that showed no statistically significant difference between normal skin and PWS lesions. Normal skin and PWS lesions can be accurately categorized by both SVM classifiers. The classifier with full feature set obtains accuracy of 92.7%, sensitivity of 92.3% and specificity of 93.8%. The classifier with simplified feature set obtains accuracy of 92.7%, sensitivity of 94.9% and specificity of 87.5%. The SVM classification results were compared with another two machine learning algorithms, random forest and decision tree. The comparison showed that SVM classifier had the best performance. Our results suggest that by training SVM classifier with quantitative features extracted from OCT images, PWS margins can be identified accurately and automatically during laser therapy.

2. Materials and Method

2.1 OCT Device

A time domain OCT system (Beijing Newraysing Laser Tech Co. Ltd., Beijing, China) based on an optic Michelson interferometer was used in this study [20]. The reason to use the time domain OCT system is that this study started in 2012 with this system. As data consistency was required by most machine learning algorithms, we captured all the data with the same system. The system uses a broadband superluminescent diode (SLED) light source (center wavelength 1310 nm; maximum output power 10 mW; bandwidth 70 nm). Four frames per second with penetration depth of around 1 mm, axial resolution of 10 um, lateral resolution of 9 um and signal-to-noise ratio of 93 dB can be achieved. The whole imaging range is 2.85 mm axial and 2.5 mm lateral with image size of 400 $\times$ 400 pixels.

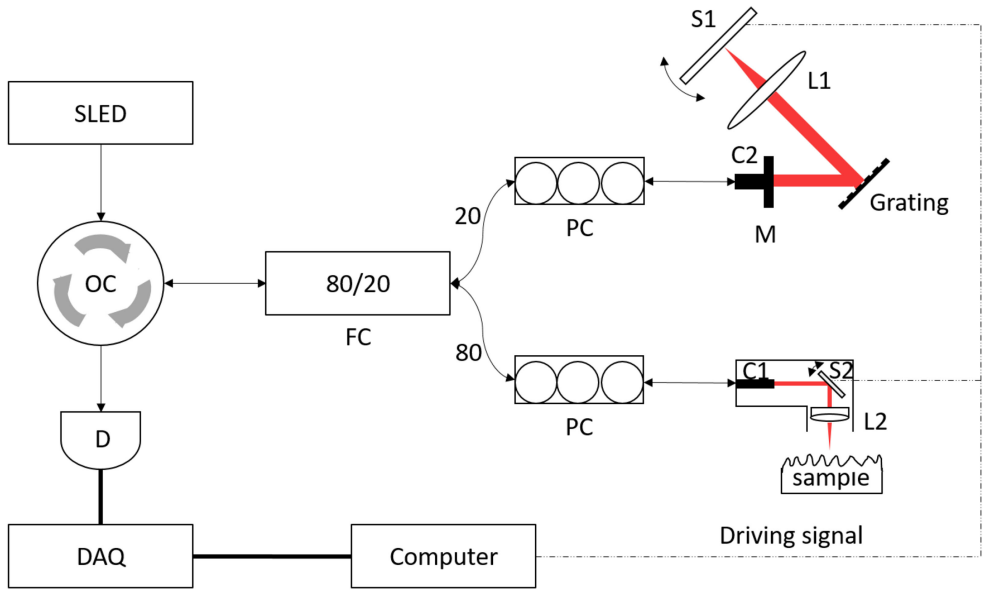

Fig. 1. Setup of the handheld OCT system. SLED: broadband superluminescent diode; OC: optical circulator; D: photodetector; DAQ: data acquisition; FC: fiber coupler; PC: polarization controller; C1, C2: collimators; S1, S2: optical scanners; L1, L2: focal lenses; M: end mirror.

2.2 Data Collection

All image samples were collected from the Chinese PLA General Hospital as part of the standard-of-care treatment for PWS. This study was approved by the PLA Postgraduate Medical School ethics board. All procedures were conducted following Ethical committee approval. 64 Chinese patients aged 2 to 23 participated in this study. All patients have PWS lesion on the face or neck area. 80 PWS sites were chosen randomly and 140 contralateral normal sites were chosen correspondingly. The number of OCT images collected varied among patients. Each site of interest was scanned 10 times in order to get repeatable results. Several OCT images of normal skin and PWS lesions were shown in Fig. 2. Orange arrows point to the vessels in the images.

2.3 Feature Extraction

The following thirteen quantitative features were extracted for classification model training. All features were chosen empirically based on formal research experience in PWS. (1) Dermal attenuation coefficient; (2) Average epidermal thickness; (3) Maximum depth of penetration; (4) Six texture features: mean, variance, entropy, speckle contrast, skewness and kurtosis. (5) Four vessel features: average vessel depth, standard deviation of vessel depth, average vessel diameter and standard deviation of vessel diameter. All these features can be grouped into three categories: Features extracted from A-scans, Features extracted from B-scans and Features extracted from vessel distributions.

2.3.1 A-Scan Based Features: One A-scan feature named dermal attenuation coefficient was extracted from average A-scan signal, which describes the decreasing rate of OCT signal along the depth within the dermal tissue. Because PWS skin has enlarged distorted blood vessels, the dermal attenuation coefficient of PWS is usually larger than the normal skin. In order to calculate this coefficient, an automated algorithm was used. First of all, we recognized the air-epidermis junction by regularized shortest path extraction [21]. After that, a threshold was used to separate the dermis and epidermis area. Dermis-epidermis junction was recognized as the first position whose value exceeds the threshold between local minimum and second maximum [21]. Fig. 1 shows the result of air-epidermis junction and dermis-epidermis junction recognition. After

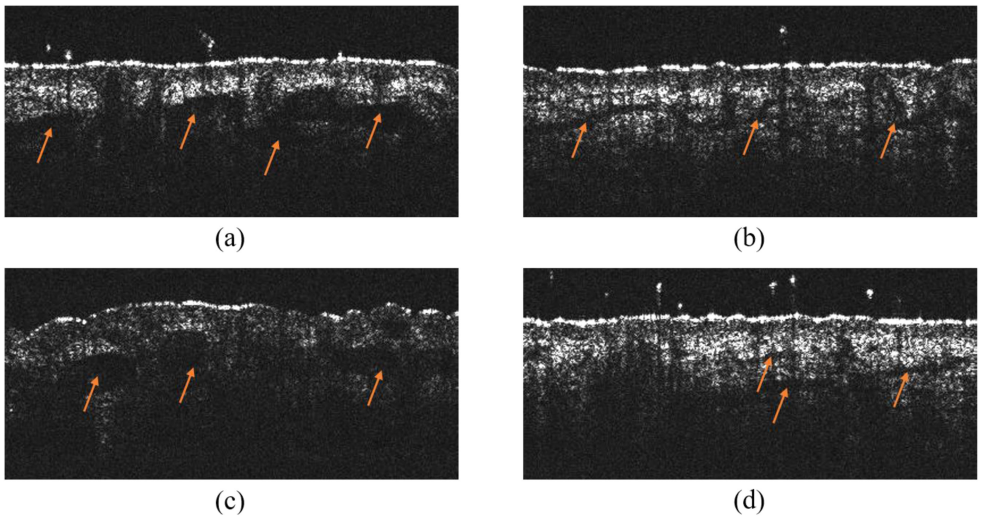

Fig. 2. OCT images of normal skin and PWS lesions. The orange arrows point to the vessels in OCT images. (a) and (c): OCT image of PWS lesions. (b) and (d): OCT image of normal skin.

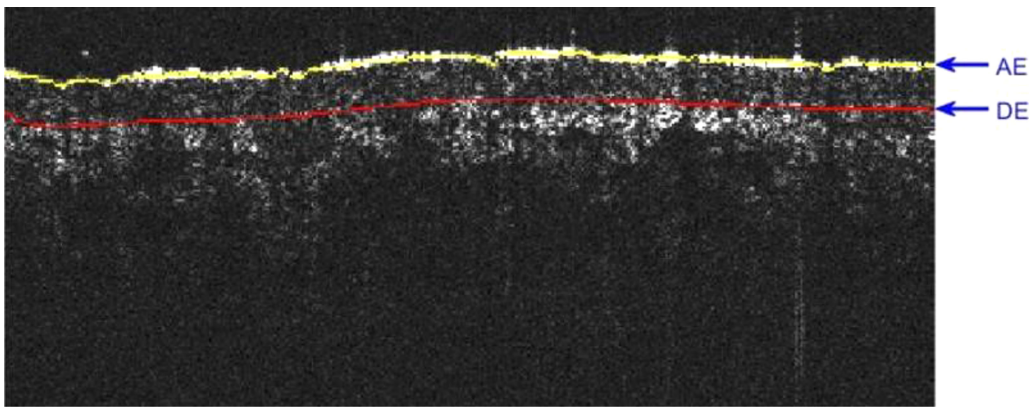

Fig. 3. Recognition of air-epidermis junction and Dermis-epidermis junction. AE: air-epidermis junction; DE: dermis-epidermis junction.

dermis-epidermis junction recognition, A-scans were shifted so that dermis-epidermis junction was at the same level as the neighboring column [22]. Then, A-scans below the dermis-epidermis junction were added and average value was computed. The average A-scan value was fitting by following equation [23]:

$$R_{(z)} = R_{(0)} e^{-2\mu_t z} + R_{bg}$$

Where, $R_{(z)}$ is the intensity in depth z; R_0 is the intensity in dermis-epidermis junction and R_{bg} is the background intensity. The attenuation coefficient μ_t describes the light decay in dermal tissue, which caused by light scattering and absorption. Fig. 3 shows the fitting results of average A-scan.

2.3.2 B-Scan Based Features: We extracted three groups of features from B-scan: average epidermal thickness, average depth of penetration and texture features.

As described above, the air-epidermis junction and dermis-epidermis junction were automatically detected. The tissue between air-epidermis junction and dermis-epidermis junction is the

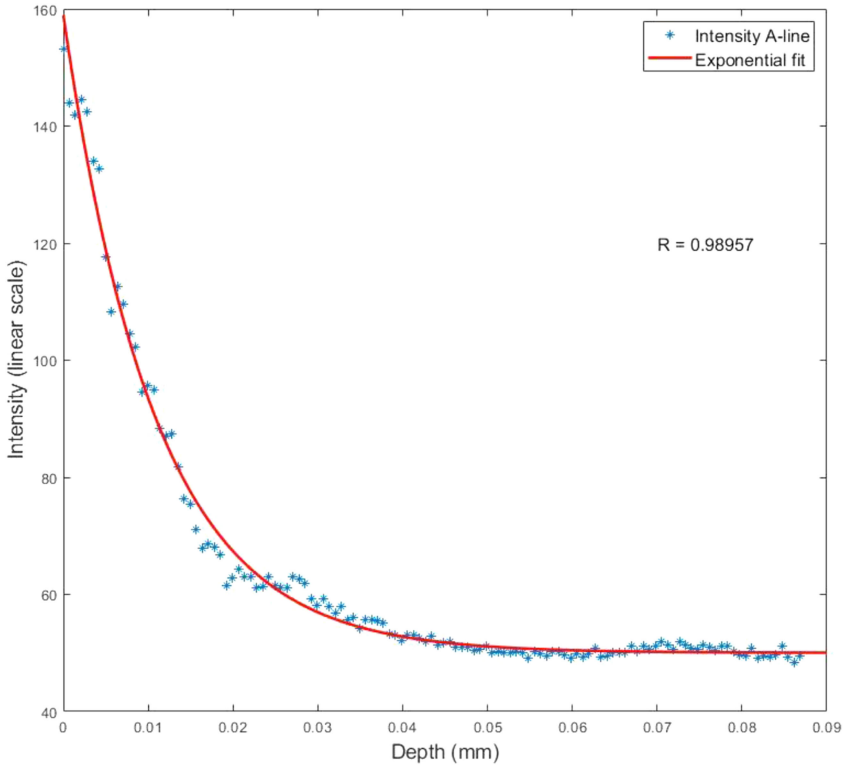

Fig. 4. Average A-scan of intensity below the dermis-epidermis junction.

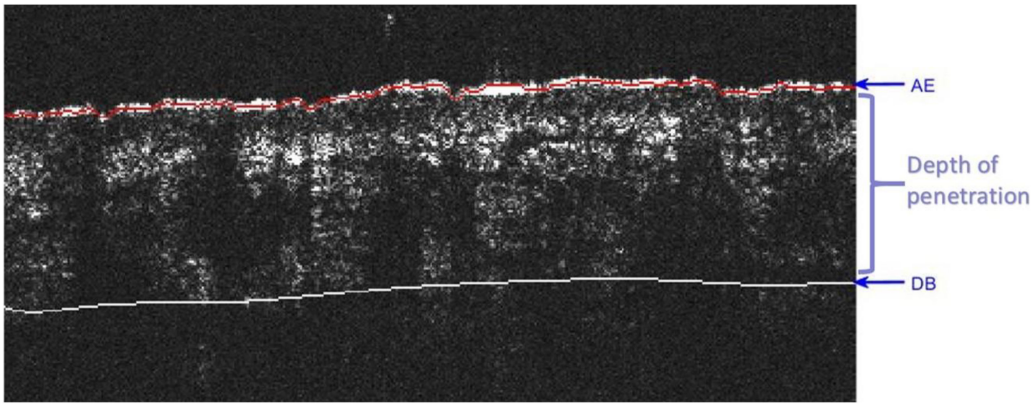

Fig. 5. Depth of penetration. AE: air-dermis junction. DB: dermis-background boundary.

epidermis. The epidermal thickness of each A-scan was measured and the average value of epidermal thickness was computed.

The optic signal decays rapidly along the axial direction. In each A-scan, the last 20 points is considered as the background intensity. We computed the average background intensity I_{bg} and standard deviation SV_{bg}. A threshold defined as $(I_{bg} + 7SV_{bg})$ was used to distinguish the dermis tissue from the background area. Fig. 5 shows the detection of air-dermis junction and dermis-background junction. Along each A-scan, the distance between the air-dermis junction and dermis-background junction was measured, which defined as the depth of penetration [21]. Then, the average value of depth of penetration was computed as a new feature.

Besides, the intensity distribution is different between normal tissue and PWS tissue, because PWS tissue contains more dilated capillary. In this work, we use six texture features such as mean, variance, entropy, speckle contrast, skewness and kurtosis. All these features can be calculated by the following formulas [24], [25]:

$$\text{Mean}\,(\mu) = \frac{1}{N}\frac{1}{M}\sum_{i=1}^{N}\sum_{j=1}^{M} x_{ij}$$

$$\text{Variance}\,(\sigma^2) = \frac{1}{N}\frac{1}{M}\sum_{i=1}^{N}\sum_{j=1}^{M}\left(x_{ij}-\mu\right)^2$$

$$\text{Entropy} = -\sum_{i=1}^{N}\sum_{j=1}^{M} p\left(x_{ij}\right)\log_2 p\left(x_{ij}\right)$$

$$\text{Speckle contrast} = \frac{\sigma}{\mu}$$

$$\text{Kurtosis} = \frac{1}{N}\frac{1}{M}\sum_{i=1}^{N}\sum_{j=1}^{M}\left[\frac{x_{ij}-\mu}{\sigma}\right]^4 - 3$$

In above formulas, N, M, x_{ij} represent the total number of pixels in the axial direction, the total number of pixels in the lateral direction and the gray level of the (i, j)th pixel, respectively. Mean is the average intensity of B-scan. Variance is the pixel intensity variance of B-scan, which measures how far the pixel intensity values spread out from their average value. Entropy describes the randomness in pixel intensity distribution. Speckle contrast is the quantified values of the mutual interference within the sample. Skewness describes the asymmetry of the pixel intensity distribution and kurtosis describes the flatness of the pixel intensity distribution [24], [25].

2.3.3 Vessel Based Features: In our previous work, blood vessel diameter and depth in each OCT B-scan were measured [17]. Four vessel based features were further extracted: average vessel depth, standard deviation of vessel depth, average vessel diameter and standard deviation of vessel diameter.

3. Model Training and Results

Data was analyzed by a homemade MATLAB program. All algorithms were implemented on a personal computer with 3.5 GHz Intel Core i3, 8GB 1600 MHz DDR3. Table 1 lists the values of features. For some features, the standard deviations are quite large compared to the mean values, because of the huge difference among patients. Pixel mean in normal skin is slightly higher than in PWS, which may be caused by the higher absorption of malformed vessel in PWS. Pixel variance, skewness and kurtosis show no significant differences between normal skin and PWS, which means that the intensity distributions of pixels were quite similar. Dermal attenuation coefficient of PWS is significantly higher than normal skin, while maximum depth of penetration of PWS is significantly lower than normal skin. Both are caused by the higher absorption of malformed vessel in PWS. Pixel entropy and speckle contrast of PWS is higher than normal skin, indicating the PWS skin becomes more heterogeneous. Average epidermal thickness of PWS is lower than normal skin, which makes the PWS skin more sensitive. Average vessel diameter and standard deviation of vessel diameter are significantly higher than normal skin, and average vessel depth is significantly lower than normal skin, which are consistent with previous results [17]. The standard deviation of vessel depth shows no significant difference between PWS and normal skin.

Thirteen quantitative features we extracted per sample were used as input features. All features were normalized before training. A support vector machine (SVM) classifier with linear kernel, a decision tree classifier using gini index and a random forests classifier of 128 decision trees were used for classification of normal and PWS tissues. The kernel of SVM classifier was chosen

TABLE 1
Features With Significant p-Values

Features	Normal skin	PWS	p-value
Dermal attenuation coefficient	36.47 ∓ 8.72	40.47 ∓ 13.99	0.0297
Average epidermal thickness	90.42 ∓ 20.61	79.97 ∓ 25.05	0.0016
Maximum depth of penetration	415.09 ∓ 48.84	379.71 ∓ 54.74	<0.00001
Mean	0.52 ∓ 0.01	0.51 ∓ 0.01	<0.00001
Variance	49.01 ∓ 0.06	49.01 ∓ 0.06	0.9263
Entropy	5.43 ∓ 0.08	5.35 ∓ 0.08	<0.000001
Speckle contrast	13.52 ∓ 0.29	13.72 ∓ 0.30	<0.00001
Skewness	19.87 ∓ 0.04	19.87 ∓ 0.04	0.5522
Kurtosis	396.41 ∓ 1.00	396.41 ∓ 1.18	0.5835
Average vessel depth	235.63 ∓ 37.80	223.11 ∓ 35.28	0.0145
Standard deviation of vessel depth	52.60 ∓ 31.07	57.20 ∓ 32.11	0.4021
Average vessel diameter	35.73 ∓ 10.25	74.58 ∓ 24.77	<0.000001
Standard deviation of vessel diameter	8.55 ∓ 6.92	20.08 ∓ 12.73	<0.000001

empirically, as linear kernel had better performance than other kinds of kernels. Other hyper parameters of these classifiers were chosen by grid search. 10 fold cross validation were used to evaluate the best hyper parameters and check the robustness of our model. Firstly, we randomly split the training set into 10 groups. For each pairs of hyper parameters, we trained the classifier ten times. Every time, we took one group out as validation set, and used the remaining groups as training set. At last, we retained all 10 evaluation scores, and computed the average value for comparison. Then we chose the best group of hyper parameters from all sets of hyper parameters. Support vector machine (SVM) is one of the most popular supervised learning methods, invented by Corinna Cortes and Vladimir Vapnik [26]. All examples are treated as high dimensional data points in space. The goal of SVM model is to find a hyperplane that separates categories by a clear gap as wide as possible. New data points are mapped into the same high dimensional space, then predicted as category based on which side of the gap they fall into. SVM can efficiently perform linear classification and non-linear classification by using kernel trick, and has good generalization ability on median-sized data set. Decision tree classifier uses a tree structure to predict the category of a target sample (classification) or to predict the value of a target variable (regression). In classification, from root to leaf, each internal node performs a test on an attribute. Each branch of the node represents an outcome of the test. Each leaf node represents a class label [33]. Decision tree can provide understandable classification rules and perform classification without requiring much computation [34]. Random forests (RF) are an ensemble machine learning method [35]. RF generates multiple decision trees and chooses the final classification having the most votes. For each decision tree, the training set is selected by Bootstrap sampling from the original training set and the features are selected randomly as the subset of the original feature set [36]. A total of 220 samples were used for classification, out of which 165 samples were used for training while 55 samples were used for testing. The ratio of sample size in training set to sample size in testing set could be chosen between 1: 1 and 9: 1 [37]–[40]. In our case, we chose the ratio to be 3: 1. Under such division, there were enough data for training and enough testing data to ensure that the results on the test set can effectively predict the classifier's performance on the new data.

In order to choose the best feature set, we trained two SVM classifiers, one trained by all 13 features, the other trained by simplified features which excluded pixel variance, skewness, kurtosis and standard deviation of vessel depth. These four features were excluded because there was no statistically significant difference between normal skin and PWS lesions for each feature. As shown in Table 1, the p-values of these features were greater than 0.05. Receiver operating characteristics (ROC) and area under the curve (AUC) were used for model evaluation. ROC shows the sensitivity against the fall-out at various threshold settings. The AUC is the area under the ROC, which describes the probability that a random positive sample is ranked higher than a random negative

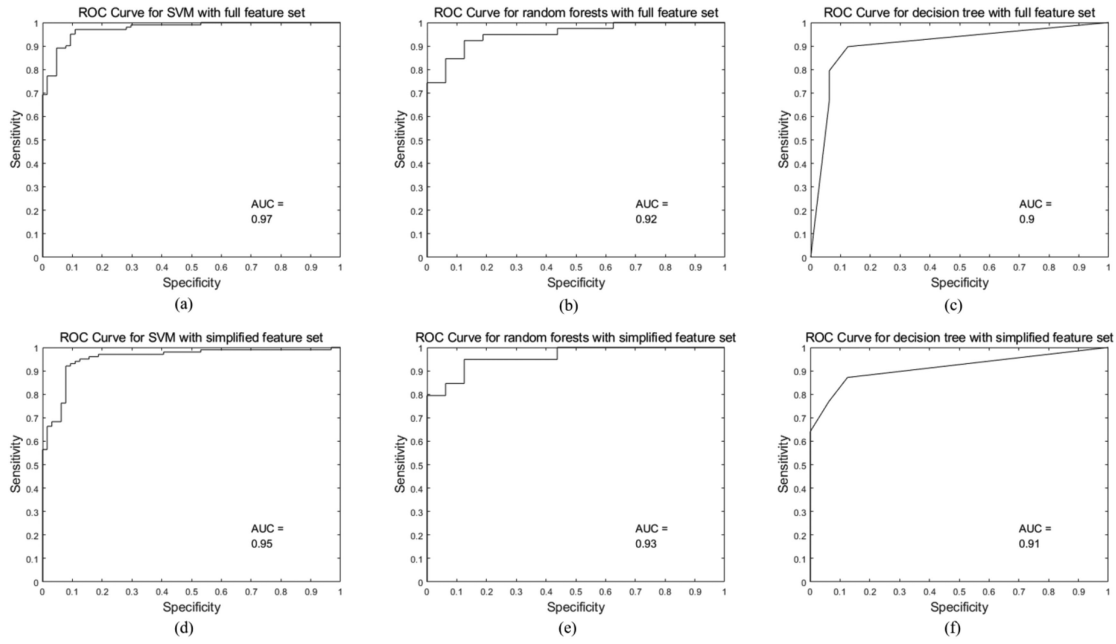

Fig. 6. ROC curve; AUC: area under the curve. (a) ROC curve for SVM classifier with full features; (b) ROC curve for random forests classifier with full features; (c) ROC curve for decision tree classifier with full features; (d) ROC curve for SVM classifier with simplified features; (e) ROC curve for random forests classifier with simplified features; (f) ROC curve for decision tree classifier with simplified features.

TABLE 2
Table of Confusion Matrix

		Classifier with full features		Classifier with simplified features	
		Predicted PWS	Predicted normal	Predicted PWS	Predicted normal
SVM	PWS	15	1	14	2
	normal	3	36	2	37
Random Forests	PWS	13	3	14	2
	normal	2	37	3	36
Decision Tree	PWS	14	2	14	2
	normal	4	35	5	34

TABLE 3
Table of Accuracy, Sensitivity and Specificity

	Classifier with full features			Classifier with simplified features		
	Accuracy	Sensitivity	Specificity	Accuracy	Sensitivity	Specificity
SVM	92.7%	92.3%	93.8%	92.7%	94.9%	87.5%
Random Forests	90.9%	94.9%	81.3%	90.9%	92.3%	87.5%
Decision Tree	89.1%	89.7%	87.5%	87.3%	87.2%	87.5%

sample. AUC varies between 0 and 1, the higher the better. Fig. 6 shows the ROC curves for all classifiers. AUC of all classifiers are greater than 0.9, which means the classifiers we get have good performance. The confusion matrix obtained by the trained classifiers on test set is shown in Table 2. Accuracy, sensitivity and specificity were calculated as ref [27], and shown in Table 3. Accuracy measures a classifier's ability to distinguish true positive and true negative cases from false positive and false negative cases. Sensitivity measures a classifier's ability to distinguish the true positive cases from the false negative cases. Specificity measures a classifier's ability to

distinguish the true negative cases from the false positive cases. Another two algorithms were used for comparison, random forest and decision tree. As shown in Table 3, all classifiers have accuracy greater than 85%. Accuracy, sensitivity and specificity in test set of SVM classifier with full features are calculated to be 92.7%, 92.3% and 93.8%, respectively. Accuracy, sensitivity and specificity in test set of SVM classifier with simplified features are 92.7%, 94.9% and 87.5%, respectively. For simplified features, the SVM classifier has the best performance in accuracy, sensitivity and specificity. For full features, the SVM classifier has best performance in accuracy and specificity. The sensitivity of SVM is slightly lower than the random forest. But the SVM classifier has balanced performance between sensitivity and specificity. The accuracy of SVM is higher than the other two classifiers. In general, the SVM classifier is better on the full feature set. Both SVM classifiers have good performance, and there is no significant difference between them, in spite of the specificity of SVM classifier with simplified features is less than the SVM classifier with full features. As shown in Table 2, SVM classifier with full features misclassifies 1 PWS lesion as normal skin and misclassifies 3 normal skin as PWS lesions. SVM classifier with simplified features misclassifies 2 PWS lesions as normal skin and misclassifies 2 normal skin as PWS lesions. It does not make much difference in terms of the number of misclassifications. The difference in sensitivity ratio and specificity ratio is mainly due to the unbalanced numbers of PWS lesions and normal skin samples in the data set. The same phenomena appear in random forests classifiers. The accuracy and sensitivity of decision tree classifier with simplified features are slightly less than the decision tree classifier with full features. As shown in Table 2, the classifier with simplified features misclassifies one more normal skin sample as PWS lesion. The results suggests that the simplified feature set provides strongly enough contrast between PWS and normal skin. In large-scale data set training, the simplified feature set can be used for good classification performance and less computing time. The feature set can be simplified further more. Because our data scale is not very large, the program runs quite fast. There is no need for further simplification up to now. But if the classifier needs to be applied on large data set, further simplification will be helpful. In this particular project, we collected 220 samples in total and achieved good classification results by using traditional machine learning algorithms. We tried deep learning methods before traditional algorithms. Two pre-trained convolutional neural network, ResNet-50 and Inception-v3 were tuned. One homemade convolutional neural network with four convolutional layers (each followed by max pooling layer) and two fully connected layers was trained. All three CNN networks had accuracies between 60% and 70%. The bad performance may be caused by small data set and large morphology variance among images in the same category. When the blood vessel running along the B-scan, it looks like a belt as shown in Fig. 1(a). When the blood vessel running perpendicular to the B-scan, it looks like an ellipse as shown in Fig. 1(c). Under the circumstances, CNN networks are not able to learn effective features in such a small data set. More samples would be helpful, and in the future project, we are going to collect more data to perform future analysis including deep learning.

4. Conclusions

In this study, 220 in vivo OCT image samples from 64 volunteers were studied. Among each image sample, thirteen quantitative features were extracted. 10 fold cross validation were used to build two SVM classifiers. The classifier with full feature set got accuracy of 92.7%, sensitivity of 92.3% and specificity of 93.8%. The classifier with simplified feature set got accuracy of 92.7%, sensitivity of 94.9% and specificity of 87.5%. Both classifiers got good performance in classification. The results indicated that classifier build by quantitative features from OCT images can be a potentially powerful tool for accurately and automatically identifying PWS margins during laser therapy.

Data Availability

The datasets analyzed in current study are available from the corresponding author on reasonable request.

References

[1] J. Jagger, "Medical lasers: Science and clinical practice," *Brit. J. Ophthalmology*, vol. 71, no. 8, 1987, Art. no. 644.
[2] M. P. Goldman and R. E. Fitzpatrick, "Cutaneous laser surgery: The art and science of selective photothermolysis," *Aorn J.*, vol. 60, no. 1, 1994, Art. no. 235.
[3] S. W. Lanigan and J. A. Cotterill, "Psychological disabilities amongst patients with port wine stains," *Brit. J. Dermatology*, vol. 121, no. 2, pp. 209–215, 1989.
[4] A. Troilius, B. Wrangsjö, and B. Ljunggren, "Potential psychological benefits from early treatment of port-wine stains in children," *Brit. J. Dermatology*, vol. 139, no. 1, pp. 59–65, 1998.
[5] J. Wang *et al.*, "Analysis of quality of life and influencing factors in 197 Chinese patients with port-wine stains," *Medicine*, vol. 96, no. 51, 2017, Art. no. e9446.
[6] S. A. Sharif *et al.*, "Noninvasive clinical assessment of port-wine stain birthmarks using current and future optical imaging technology: A review," *Brit. J. Dermatology*, vol. 167, no. 6, pp. 1215–1223, 2012.
[7] Z. F. Jasim and M. H. Julian, "Treatment of pulsed dye laser–resistant port wine stain birthmarks," *J. Amer. Acad. Dermatology*, vol. 57, no. 4, pp. 677–682, 2007.
[8] D. Huang *et al.*, "Optical coherence tomography," *Science*, vol. 254, no. 5035, pp. 1178–1181, 1991.
[9] E. C. Sattler, R. Kästle, and J. Welzel, "Optical coherence tomography in dermatology," *J. Biomed. Opt.*, vol. 18, no. 6, 2013, Art. no. 061224.
[10] D. Chen *et al.*, "Relationship between the blood perfusion values determined by laser speckle imaging and laser Doppler imaging in normal skin and port wine stains," *Photodiagnosis Photodynamic Therapy*, vol. 13, pp. 1–9, 2016.
[11] T. Lister, P. Wright, and P. Chappell, "Spectrophotometers for the clinical assessment of port-wine stain skin lesions: A review," *Lasers Med. Sci.*, vol. 25, no. 3, pp. 449–457, 2010.
[12] S. Astner *et al.*, "Preliminary evaluation of benign vascular lesions using in vivo reflectance confocal microscopy," *Dermatologic Surgery*, vol. 36, no. 7, pp. 1099–1110, 2010.
[13] M. D. Shriver and E. J. Parra, "Comparison of narrow-band reflectance spectroscopy and tristimulus colorimetry for measurements of skin and hair color in persons of different biological ancestry," *Amer. J. Phys. Anthropology: Official Publication Amer. Assoc. Phys. Anthropologists*, vol. 112, no. 1, pp. 17–27, 2000.
[14] B. Jung *et al.*, "Characterization of port wine stain skin erythema and melanin content using cross-polarized diffuse reflectance imaging," *Lasers Surgery Med.*, vol. 34, no. 2, pp. 174–181, 2004.
[15] Y. C. Huang *et al.*, "Blood flow dynamics after laser therapy of port wine stain birthmarks," *Lasers Surgery Med.: Official J. Amer. Soc. Laser Med. Surgery*, vol. 41, no. 8, pp. 563–571, 2009.
[16] A. Mazhar *et al.*, "Spatial frequency domain imaging of port wine stain biochemical composition in response to laser therapy: A pilot study," *Lasers Surgery Med.*, vol. 44, no. 8, pp. 611–621, 2012.
[17] S. Zhao *et al.*, "Imaging port wine stains by fiber optical coherence tomography," *J. Biomed. Opt.*, vol. 15, no. 3, 2010, Art. no. 036020.
[18] D. Huang *et al.*, "Optical coherence tomography," *Science*, vol. 254, no. 5035, pp. 1178–1181, 1991.
[19] E. C. Sattler, R. Kästle, and J. Welzel, "Optical coherence tomography in dermatology," *J. Biomed. Opt.*, vol. 18, no. 6, 2013, Art. no. 061224.
[20] T. S. Wang *et al.*, "Handheld optical coherence tomography device for photodynamic therapy," *Chin. Sci. Bull.*, vol. 57, no. 5, pp. 450–454, 2012.
[21] C. Wang *et al.*, "Automated assessment of epidermal thickness and vascular density of port wine stains OCT image," *J. Innovative Opt. Health Sci.*, vol. 7, no. 1, 2014, Art. no. 1350052.
[22] A. M. Bagci *et al.*, "Thickness profiles of retinal layers by optical coherence tomography image segmentation," *Amer. J. Ophthalmology*, vol. 146, no. 5, pp. 679–687, 2008.
[23] L. Scolaro *et al.*, "Parametric imaging of the local attenuation coefficient in human axillary lymph nodes assessed using optical coherence tomography," *Biomed. Opt. Express*, vol. 3, no. 2, 2012, Art. no. 366.
[24] A. Butola *et al.*, "Volumetric analysis of breast cancer tissues using machine learning and swept-source optical coherence tomography," *Appl. Opt.*, vol. 58, no. 5, pp. A135–A141, 2019.
[25] N. Singla, V. Srivastava, and D. S. Mehta, "In vivo classification of human skin burns using machine learning and quantitative features captured by optical coherence tomography," *Laser Phys. Lett.*, vol. 15, no. 2, 2018, Art. no. 025601.
[26] C. Cortes and V. Vapnik, "Support-vector networks," *Mach. Learn.*, vol. 20, no. 3, pp. 273–297, 1995.
[27] W. Zhu, N. Zeng, and N. Wang, "Sensitivity, specificity, accuracy, associated confidence interval and ROC analysis with practical SAS implementations," in *Proc. NESUG: Health Care Life Sci.*, 2010, vol. 19, pp. 67–75.
[28] L. Duan *et al.*, "Automated identification of basal cell carcinoma by polarization-sensitive optical coherence tomography," *Biomed. Opt. Express*, vol. 5, no. 10, pp. 3717–3729, 2014.
[29] T. Marvdashti *et al.*, "Classification of basal cell carcinoma in human skin using machine learning and quantitative features captured by polarization sensitive optical coherence tomography," *Biomed. Opt. Express*, vol. 7, no. 9, pp. 3721–3735, 2016.
[30] L. P. Rangaraju *et al.*, "Classification of burn injury using Raman spectroscopy and optical coherence tomography: An ex-vivo study on porcine skin," *Burns*, vol. 45, pp. 659–670, 2018.
[31] A. Butola *et al.*, "Volumetric analysis of breast cancer tissues using machine learning and swept-source optical coherence tomography," *Appl. Opt.*, vol. 58, no. 5, pp. A135–A141, 2019.
[32] F. Bazant-Hegemark, *et al.*, "Optical coherence tomography: A potential tool for unsupervised prediction of treatment response for port-wine stains," *Photodiagnosis Photodynamic Therapy*, vol. 5, no. 3, pp. 191–197, 2008.
[33] C. Bird, T. Menzies, and T. Zimmermann, Eds., *The Art and Science of Analyzing Software Data*. Amsterdam, The Netherlands: Elsevier, 2015.
[34] D. Talia, P. Trunfio, and F. Marozzo, *Data Analysis in the Cloud: Models, Techniques and Applications*. Amsterdam, The Netherlands: Elsevier, 2015.
[35] L. Breiman, "Random forests," *Mach. Learn.*, vol. 45, no. 1, pp. 5–32, 2001.

[36] R. Pal, *Predictive Modeling of Drug Sensitivity*. Orlando, FL, USA: Academic, 2016.
[37] S. P. K. Karri, D. Chakraborty, and J. Chatterjee, "Transfer learning based classification of optical coherence tomography images with diabetic macular edema and dry age-related macular degeneration," *Biomed. Opt. Express*, vol. 8, no. 2, pp. 579–592, 2017.
[38] Y. Wang *et al.*, "Machine learning based detection of age-related macular degeneration (AMD) and diabetic macular edema (DME) from optical coherence tomography (OCT) images," *Biomed. Opt. Express*, vol. 7, no. 12, pp. 4928–4940, 2016.
[39] K. J. Halupka *et al.*, "Retinal optical coherence tomography image enhancement via deep learning," *Biomed. Opt. Express*, vol. 9, no. 12, pp. 6205–6221, 2018.
[40] L. Huang *et al.*, "Automatic classification of retinal optical coherence tomography images with layer guided convolutional neural network," *IEEE Signal Process. Lett.*, vol. 26, no. 7, pp. 1026–1030, 2019.